

Universal features of the jamming phase diagram of wet granular materials

S. H. Ebrahimpnazhad Rahbari,^{1,2,*} M. Khadem-Maaref,¹ and S. K. A. Seyed Yaghoubi³

¹*Faculty of Physics, Plasma and Condensed Matter Computational Lab, Shahid Madani University of Azarbayjan, Tabriz, Iran*

²*Department of Complex Fluids, Max-Planck Institute for Dynamics and Self-Organization, 37073 Göttingen, Germany*

³*Department of Theoretical Physics, Faculty of Physics, University of Tabriz, Tabriz, Iran*

(Received 24 April 2013; revised manuscript received 3 July 2013; published 23 October 2013)

We investigate the influence of the shape of a particle on the structure of the jamming phase diagram of wet granular materials. We compute the jamming phase diagram of wet dimers (two fused disks) and compare it with that of the wet disks. Amplitude of the external force at solidification, i.e., the jamming force F_s , is computed as a function of the packing fraction ϕ , the capillary bridge energy ε , and the aspect ratio of dimers α . Based on data collapse, an equation for amplitude of the external force at solidification $F_s(\phi, \varepsilon, \alpha)$ is derived. F_s has scaling and logarithmic relations with ϕ and ε , respectively, exactly the same type reported for wet disks earlier. Interestingly, F_s does not depend on the aspect ratio of dimers α . The only difference is that wet dimers are found to be more stiffer than wet disks. However, the similarities of the equations describing $F_s(\phi, \varepsilon, \alpha)$ of wet dimers and disks imply that there exists, yet unknown, universal aspects of mechanical response of wet granular materials to the external forces, independent from the particle shape. In addition, we study local orientation of particles and its statistical properties.

DOI: [10.1103/PhysRevE.88.042203](https://doi.org/10.1103/PhysRevE.88.042203)

PACS number(s): 45.70.-n, 61.43.Hv, 47.57.eb, 66.10.C-

I. INTRODUCTION

Liu and Nagel [1] have proposed that dynamic arrest of soft materials such as foams and granular particles together with glassy systems undergoing glass transition possess a universal phase diagram called the *jamming phase diagram*. O'Hern *et al.* [2] have explored the jamming phase diagram of frictionless bidisperse disks and have shown that at zero temperature and at zero applied stress there exists a well-defined point, the J point, above which the system develops yield stress. On the other hand, Olsson *et al.* [3] have shown that when the J point is approached from a flowing regime, the crossover into the jammed state is a true second-order-like phase transition. Simulations of the jamming of frictional disks have shown that the structure of the jamming phase diagram can depend on interactions between particles [4]. It is also known that in the jammed systems, force chains are responsible for development of yield stress [5]. Furthermore, topology of the network of the force chains in granular materials is known to depend on the particle shape [6,7]. Other studies have revealed the influence of the particle shape on the jamming transition of nonspherical particles, while only little has been understood about the influence of the particle shape. It is shown that jamming of frictionless ellipsoids have fundamentally different dynamic exponents from those of spherical particles [8]. However, measurements of yield stress of dimers and ellipsoids revealed that the yield stress is independent of convexity or concavity of dry granular particles [9].

Properties of granular materials change dramatically when a small portion of liquid is added [10,11]. Due to capillary bridges between particles, wet granular matter can develop yield stress well below the random close packing (RCP) limit. Accordingly, the current methods which study jamming of dry granulates do not seem to be appropriate for wet particles, therefore different methods should be introduced.

To this end, we have developed a method based on applying a heterogeneous driving force into the system [12]. We have shown that for wet disks, even well below the RCP, there exists a well-defined threshold for the amplitude of the external force below which the system develops yield stress and transits into a solidified quiescent state. Based on data collapse, we have also found that the solidification force scales with the packing fraction ϕ and has a logarithmic relation with the capillary energy ε . In this manuscript, we will provide an answer to the question if the microstructural properties of wet granular materials can influence their jamming phase diagram. For our purpose, we calculate the jamming phase diagram of wet dimers and compare it with the one obtained for wet disks. We find that the structure of the jamming phase diagram does not change when wet disks are replaced with wet dimers, hence, we get exactly the same relations as we have obtained for wet disks.

This paper is organized as follows: in Sec. II we elucidate basic properties of wet granular materials in the capillary bridge regime, how we model the capillary interactions, the numerical implementation for simulations, and preparation of the initial packings. In Sec. III we present results of extensive MD-type simulations of wet rigid dimers driven by a sinusoidal force whose wavelength agrees with the length of the simulation box. This section opens with snapshots of the solidified (jammed) and fluidized states to give an instantaneous perception on these complex states. Next, we present profiles of the drift velocity V_y , the shear rate $\dot{\gamma}$, and components of the stress tensor σ . Furthermore, we show how the jamming point is measured and how the jamming phase diagram of wet dimers is computed by measuring the solidification point F_s as function of the packing fraction ϕ , the capillary energy ε , and the aspect ratio of dimers α . In Sec. IV, we address the similarities and differences of the jamming phase diagram of wet disks and dimers. Finally, the paper is closed in Sec. IV where the relation of the amplitude of the external force at solidification F_s and the system size

*habib.rahbari@gmail.com

L is calculated by an analytical line of argument based on the theory given in Ref. [12].

II. MODEL

The capillary bridges between particles in wet granular materials are responsible for stiffness of the system [10,13–17]. A capillary bridge forms instantaneously when two particles touch one another, while thin films of liquid have already covered their surfaces before the collision. The capillary bridge forms at the contact point of two colliding particles and the resulting bridge entails an attractive force F_c . When distance between two particles exceeds a critical value s_c , the capillary bridge ruptures and some energy ε dissipates

$$\varepsilon = \int_0^{s_c} F_c ds. \quad (1)$$

The dissipation is due to the hysteretic nature of the capillary interactions and there is no other source of dissipation in the current study.

A. Interactions

We investigate the influence of two types of interactions on the collective behavior of wet granular materials under shear. (i) Capillary interactions: We consider a minimal capillary model in which the capillary force F_c is constant, as the distance between particles changes [10]. In the simulations, the minimal capillary force, F_c , is used as a force scale and the capillary bridge energy, ε , is the only free parameter determining the effect of the capillary bridges. (ii) Repulsive interactions: Mutual repulsion between the monomers is modeled by a soft-core nonlinear spring [2] giving rise to a repulsive force,

$$F_r(r_{ij}) = \begin{cases} C_{ij}(R_i + R_j - r_{ij})^{1/2} & \text{for } r_{ij} \leq R_i + R_j \\ 0 & \text{otherwise,} \end{cases} \quad (2a)$$

where r_{ij} is the Euclidean distance between the center of monomer i and j . In the spirit of Hertz's contact law [18] we set

$$C_{ij} = C \left(\frac{R_i R_j}{R_i + R_j} \right)^{1/2} \quad (2b)$$

in order to account for different monomer radii. The global parameter C controls the hardness of the monomers.

Newton's equation of motion for dimer i reads

$$m_i \frac{d^2 \mathbf{r}_i}{dt^2} = \sum_{j \in \mathcal{N}(i)} \mathbf{e}_{ij} f_{ij}(r_{ij}), \quad (3)$$

where $m_i = (m_1 + m_2)_i$ is sum of the masses of its two monomers, \mathbf{r}_i is the position of center of mass of dimer i , $\mathcal{N}(i)$ is the set of neighbors j interacting with i , the unit vector \mathbf{e}_{ij} points from the center of dimer i to the center of dimer j , and f_{ij} is the force exerted by dimer i on dimer j . The latter force comprises the soft-core repulsion 2, and whenever applicable also the attractive force, F_c , modeling capillary bridges. Equation (3) is solved numerically for both translational and rotational degrees of freedom using a fifth-order predictor-corrector Gear algorithm.

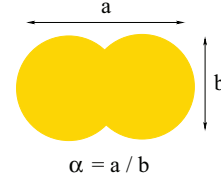


FIG. 1. (Color online) Sketch of a dimer. A dimer is formed by fusion of two disks. For a and b as the length of the major and minor axes, the aspect ratio α is defined as a divided by b . We vary the aspect ratio in the range $1 < \alpha < 2$ in our simulations. The rotational and translational equations of motion are solved for center of mass of the dimers numerically.

B. Numerical implementations

We perform MD-type simulations of 2D wet bidisperse rigid dimers. Periodic boundary conditions are applied into both directions. As a simplest example of concave particles, we simulate wet dimers by fusing two wet disks. A sketch of a dimer is shown in Fig. 1. For a and b as the length of the major and minor axes, the aspect ratio of a dimer α is defined as $\alpha = a/b$, and we vary the aspect ratio in the range $1 < \alpha < 2$. Furthermore, the RCP limit of dimers is a function of the aspect ratio α and is given in Fig. 1 and Ref. [9]. Accordingly, the packing fraction at the onset of jamming for dry dimers ϕ_j is a monotonically increasing function of the aspect ratio in the range $1 < \alpha < 1.4$, where $\phi_j(\alpha = 1) \simeq 0.84$ and $\phi_j(\alpha = 1.4) \simeq 0.8852$, whereas ϕ_j is a monotonically decreasing function of the aspect ratio for $\alpha > 1.4$ where the largest reported aspect ratio is $\phi_j(\alpha = 1.9) \simeq 0.86$. The reason for such increase of ϕ_j is that as the aspect ratio α becomes larger than 1, the number of contacts per particle increases, and thus the packing fraction at the onset of jamming ϕ_j is increased. The decrease of ϕ_j for $\alpha > 1.4$ is a direct consequence of the enhanced exclusion-volume of orientationally disordered packings of elongated particles [19].

In order to prevent crystallization, we have a 2:1 mixture of small and large dimers where the ratio of minor axes of the large and small dimers is set to 1.4. As mentioned before, we consider two kinds of interactions in the simulations: First, the capillary interaction due to the capillary bridges between particles in the system for which we engage the minimal capillary force and, second, a repulsive force among particles acts when they collide and deform (or numerically overlap). The repulsive force is given by Eq. (2), which describes a nonlinear spring force.

Particles are driven by a spatially heterogeneous force that reproduces the effects of shearing with gravity. Following Ref. [12], the external force $\mathbf{F}_{\text{ex}}(\mathbf{x})$ reads

$$\mathbf{F}_{\text{ex}}(\mathbf{x}) = \mathbf{e}_y F_e \cos(2\pi x/L). \quad (4)$$

This force is applied at the center of mass of individual dimers. The order parameter Δv_y is chosen as the difference of the drift velocity v_y of particles in a narrow column along the flow at $x = 0$ and $x = L/2$, while the control parameter is the amplitude of the external force F_e . When the system develops yield stress and solidifies, we obtain $\Delta v_y = 0$; otherwise, in a fluidized state, $\Delta v_y \neq 0$.

Granular temperature T_G is defined as the mean fluctuating kinetic energy of particles,

$$T_G = \frac{1}{N} \sum_{i=1}^N \frac{1}{2} m_i ((v_y^i - U_y(x))^2 + (v_x^i)^2), \quad (5)$$

where $v_y^i - U_y(x)$ is the y component of the velocity of particle i subtracted from the local drift velocity $U_y(x)$ at the spatial position x . Since the external force is along the y direction, the mean drift velocity along x direction is zero.

We utilize the Lubachevsky-Stillinger algorithm [20] to prepare initial packings for simulations. More details about the preparation of initial packings is given at Ref. [12]. Assuming a constant mass per area, ρ , the individual mass of dimer i equals its area. Throughout the remainder of this paper, we employ dimensionless rescaled quantities based on the capillary force, F_c , the mass density of the dimers, ρ , and the average of minor axes of large and small dimers D . Time, t , and mass, m , are, hence, measured in units $\tau \equiv \sqrt{\rho D^3 / F_c}$ and $\mu \equiv \rho D^2$, respectively. Using these normalized quantities, it is straightforward to normalize all physical quantities derived from mass, length, and time, such as the local averages of velocities and the shear rate.

III. RESULTS

A. Solidified (jammed) and fluidized states

Snapshots of the system are shown in Fig. 2. The top and bottom figures show the solidified and fluidized states, respectively. In the solidified state, the system has settled down into a homogeneous stable state. If zoomed in, the capillary bridges between particle can be seen by the blue color. The force chains, shown by the black cylinders with the diameter dependent on the magnitude of the interparticle forces, form vortexlike patterns. In the fluidized state, the system is heterogeneous, i.e., dilute at $x = L/4$ and $3L/4$, where random motion of particles are highest and, according to Eq. (5), the granular temperature T_G has maxima, and is dense at $x = 0$ and $L/2$, where particles have a pluglike drift with very little random motion inferring that T_G has minima. Two maxima of the granular temperature T_G at $x = L/4$ and $3L/4$ are accompanied by maxima of the shear stress at the same positions which is explicitly predicted by Eq. (9).

The structure of force chains in the fluidized state has hierarchical patterns and differs from the one in the solidified state.

B. Temporal evolution of the order parameter Δv_y

The order parameter is given by

$$\Delta v_y = \frac{1}{2} [v_y(x=0) - v_y(x=L/2)], \quad (6)$$

where $v_y(x)$ shows the average drift velocity of particles at the lateral position x , along the flow direction in a narrow column where the amplitude of the external force can be considered constant. Figure 3 shows the order parameter Δv_y vs time for six solidified and fluidized states, from bottom to top, respectively. One can see that for solidified states, after some rearrangements of the particles, which takes until $t = 30$, the system develops yield stress and the order parameter becomes

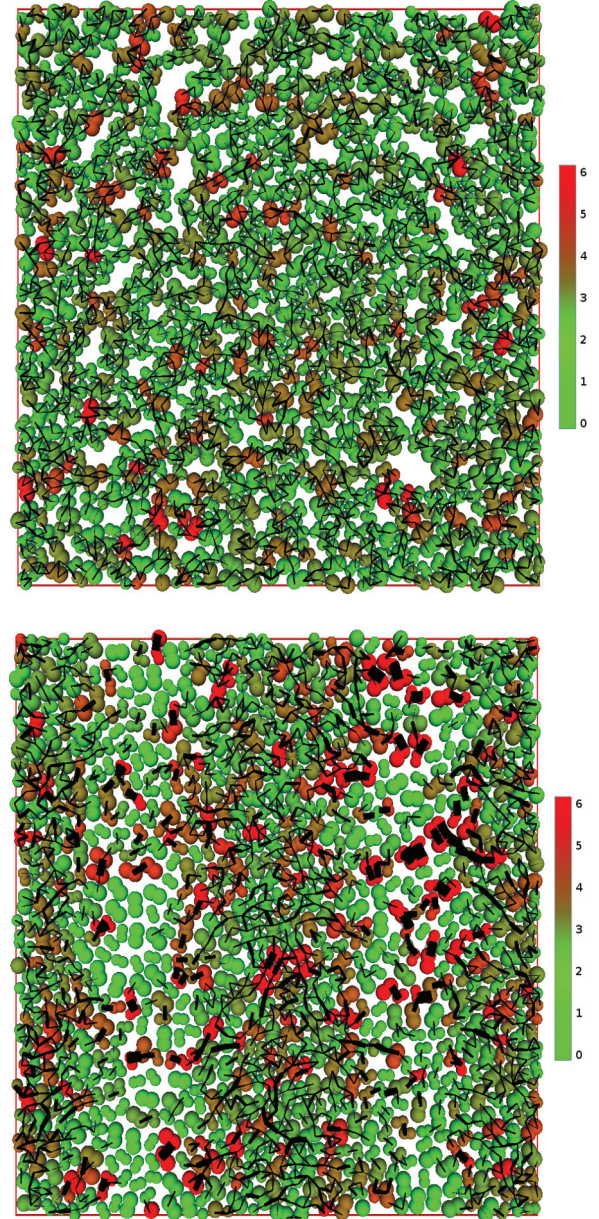


FIG. 2. (Color online) Sketch of the system for both solidified (top) and fluidized (bottom) states. The color code of particles shows total magnitude of interparticle forces exerted by neighbors to the particles ranging from 0 (green) to 6 (red). If zoomed in, capillary bridges between particles with blue color can be seen. The force chains are illustrated with black cylinders, each of which has a width proportional to magnitude of the interparticle force. Top: Amplitude of the external force is $F_e = 5 \times 10^{-3}$. The system has attained a homogeneous state where the green and red particles are uniformly distributed. Bottom: Amplitude of the external force is $F_e = 1 \times 10^{-2}$. The system is visibly heterogeneous. The packing fraction is $\phi = 0.8$, the aspect ratio is $\alpha = 1.6$, the capillary energy is $\varepsilon = 0.05$, the system size is $L = 40$, and the number of dimers is $N = 2070$ (see the Supplemental Material for two movies of our simulations for the solidified and fluidized states [21]).

zero in average. However, when $F_e > F_s$, the system settles down into a dynamic stationary state where Δv_y becomes nonzero in average. This is how we find the transition point for a given configuration.

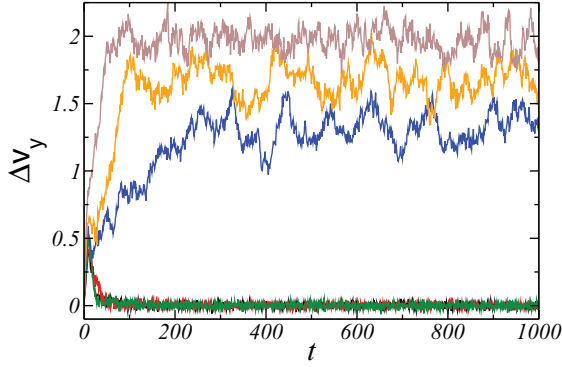


FIG. 3. (Color online) Temporal evolution of the order parameter Δv_y for six different amplitude of the external force $F_e = 1.15 \times 10^{-2}$, 1.7×10^{-2} , 1.9×10^{-2} , 2.33×10^{-2} , 3×10^{-2} , and 4×10^{-2} from bottom to top, respectively. In the first three curves, representing the solidified states, the average value of the order parameter is $\Delta v_y = 0$. For the rest of the curves, where the system is fluidized, the order parameter converges to a nonzero value. In these simulations, the packing fraction is $\phi = 0.7$, the capillary energy is $\varepsilon = 0.05$, the aspect ratio of dimers is $\alpha = 1.5$, and the system size is $L = 20$.

C. Jamming and fluidization transitions

Figure 4 shows the dependence of the order parameter Δv_y as function of the control parameter F_e . In these simulations, the packing fraction is $\phi = 0.7$, the aspect ratio is $\alpha = 1.5$, the capillary energy is $\varepsilon = 0.05$, and the system size is $L = 20$. We start from a fluidized state (red symbols) far from the solidification point at value $F_e = 6.2 \times 10^{-2}$ and decrease F_e stepwise until it solidifies at value $F_s = 2.2 \times 10^{-2}$. Then we increase the driving force amplitude F_e stepwise until it refluidizes at the value $F_f = 2.85 \times 10^{-2}$. Both transitions are discontinuous with large hysteresis resembling subcritical

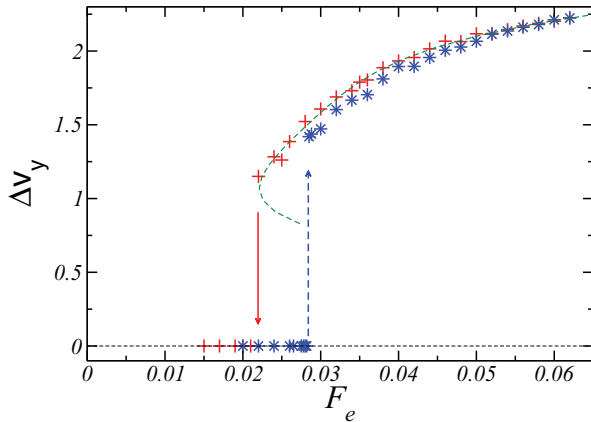


FIG. 4. (Color online) The order parameter Δv_y as function of the control parameter F_e . We start at value $F_e = 6.2 \times 10^{-2}$, where the system settles down into a fluidized state, and we decrease F_e stepwise until it solidifies at $F_s = 2.2 \times 10^{-2}$. Then we increase the driving force amplitude F_e , until the system refluidizes at value $F_f = 2.85 \times 10^{-2}$. Both transitions are discontinuous with large hysteresis resembling a subcritical bifurcation. Both paths follow similar trends. In these simulations, the packing fraction is $\phi = 0.7$, the aspect ratio is $\alpha = 1.5$, the capillary energy is $\varepsilon = 0.05$, and the system size is $L = 20$.

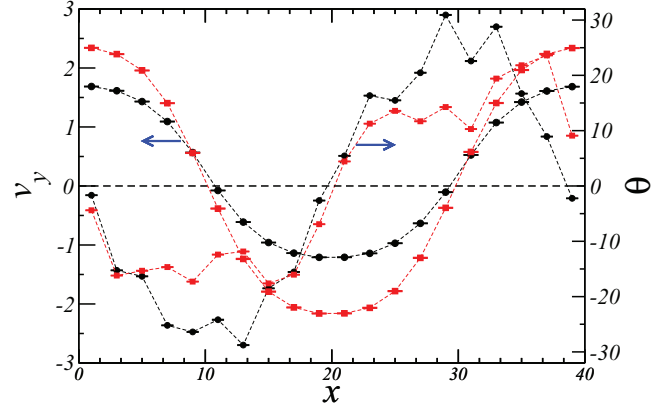


FIG. 5. (Color online) Profiles of the average local drift v_y (curves indicated by arrow pointing to the left scale) and average orientation of particles θ (curves indicated by arrow pointing to the right scale), with respect to the vertical direction. The black and red symbols correspond to values $F_e = 3.3 \times 10^{-2}$ and 6×10^{-2} , respectively. Local orientation of particles is not random and depends systematically on the lateral position of particles and amplitude of the external force F_e . In these simulations, the packing fraction is $\phi = 0.7$, the aspect ratio is $\alpha = 1.8$, the capillary energy is $\varepsilon = 0.05$, and the system size is $L = 40$.

bifurcation transition with an unstable branch below the solidification point. This is in contrast to dry granular matter in which the jamming transition is continuous. Both F_s and F_f are found to be larger than those obtained for wet disks with the same ϕ and ε [12], implying that wet dimers are stiffer than wet disks.

D. Velocity and orientation profiles

In the solidified state, the system is almost homogeneous, while in the fluidized state the system becomes extremely heterogeneous: (i) dense at $x = 0$ and $L/2$, where the granular temperature T_G and the shear rate $\dot{\gamma}$ have minima, and (ii) loose at $x = L/4$ and $3L/4$, where T_G and $\dot{\gamma}$ have maxima. Figure 5 shows profiles of the local drift velocity v_y and the average orientation of the dimers θ . In this simulation, the area fraction is $\phi = 0.7$, the capillary energy is $\varepsilon = 0.05$, the aspect ratio of dimers is $\alpha = 1.8$, and the box size is $L = 40$. All the local parameters are calculated along columns where F_e takes constant values. We start to measure physical quantities in $t = 1000$, up to which the system has already been settled down into a stationary state, and continue measuring them up until $t = 2000$. Each profile is an average over 1000 equidistance profiles in time. It is observed that the velocity profile strictly depends on the shape of the driving force and attains a cosinike shape. The black and red symbols in Fig. 5 correspond to the values $F_e = 3.3 \times 10^{-2}$ and 6×10^{-2} . The average local orientation of particles with respect to the flow direction seems to be the highest, $\theta \approx 30$, at $x = 10$ and 30 , where the shear rate becomes maximal, and almost zero at $x = 0$ and 20 , where the shear rate becomes zero. The overall distribution of orientation of the dimers and the spatial correlation of the orientation of particles are given in the next subsection.

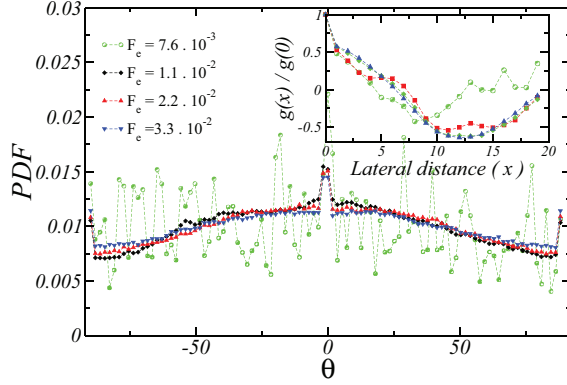


FIG. 6. (Color online) PDF of orientation of dimers θ , with respect to the vertical direction averaged over all the particles in the system. The light-green symbols show the PDF of θ for a solidified state in which $F_e = 7.6 \times 10^{-3}$. All the points scatter uniformly between the two limits. However, for the black, red, and blue symbols where the system is fluidized and the amplitude of the external force is $F_e = 1.1 \times 10^{-2}$, 2.2×10^{-2} , and 3.3×10^{-2} , respectively, the distribution has a peak at $\theta = 0$ and it monotonically decreases away from the peak. Inset: The correlation function $g(x)/g(0)$ versus the spatial position x is shown for solidified and fluidized states (more information provided in the main text). In these simulations the packing fraction is $\phi = 0.7$, the aspect ratio of dimers is $\alpha = 1.8$, the capillary energy is $\varepsilon = 0.05$, and the system size is $L = 40$.

E. Statistics of local orientation of dimers

Figure 6 shows the probability distribution of orientation of dimers in the system. In this simulation, the packing fraction is $\phi = 0.7$, the aspect ratio of dimers is $\alpha = 1.8$, the capillary energy is $\varepsilon = 0.05$, and the system size is $L = 40$. The orientation of the particles is calculated with respect to the y axis and it is averaged over all values of x . The orientation of the particles θ varies in the range $-90^\circ < \theta < +90^\circ$. The light-green symbols show the PDF of θ for a solidified state in which $F_e = 7.6 \times 10^{-3}$. All the symbols scatter randomly between the range $-90^\circ < \theta < +90^\circ$, without any systematic dependence on the lateral position x . However, for the black, red, and blue symbols, where the system is fluidized, the distribution has a peak at $\theta = 0$, and it goes down monotonically away from the peak. One can see that the distributions of the orientation θ , in solidified and fluidized states, dramatically differ. The inset in Fig. 6 depicts the correlation function $g(x)/g(0)$, where $g(x) = \langle \theta(r)\theta(r+x) \rangle$, and x is the lateral distance between two dimers. In the fluidized state, the correlation function decreases on increasing the lateral distance between two dimers x and develops a minimum at around $x = 12.5$. One may interpret the position of the minimum as the correlation length for θ . Accordingly, the correlation length in the fluidized state does change on increasing the amplitude of the external force F_e . Also, the correlation length in the solidified state is smaller than in the fluidized state.

F. Balance of interparticle and external forces

As a result of the balance of the external force with internal stress, in both solidified and fluidized states, when the system

reaches the stationary state, we expect to have

$$\nabla \cdot \sigma = \mathbf{f}, \quad (7)$$

where σ is the stress tensor and \mathbf{f} is the external driving force per unit volume (this is a simplified version of the Navier-Stokes equation). For $\mathbf{f} = NF_e/A \cos(2\pi x/L)\hat{e}_y$, being the density of the external force, we get

$$\frac{\partial S_{xy}}{\partial x} = \frac{NF_e}{A} \cos \frac{2\pi x}{L}, \quad (8)$$

where S_{xy} is the off-diagonal component of the stress tensor σ , N is the number of dimers, and L is the system size. After integration, we obtain

$$S_{xy} = \frac{NF_e}{2\pi L} \sin \frac{2\pi x}{L}, \quad (9)$$

where we have supposed that particles are uniformly distributed in the system, and the area of the system equals $A = L^2$, and N is the number of dimers in the system. Figure 7 (top) shows profiles of the stress tensor for solidified and fluidized states where the amplitude of the external force has values $F_e = 7.6 \times 10^{-3}$ and 2.2×10^{-2} , respectively. The blue and maroon symbols show the simulation data, and the orange solid lines show the prediction by Eq. (9). One can see that the internal stress has counterbalanced the external force. Figure 7 (bottom) shows the corresponding S_{xx} and S_{yy} for both states. Since there is no external force applied along the x direction, S_{xx} should be constant throughout the system, which is in accord with the data obtained from the simulations. In the fluidized state, S_{yy} has two maxima, where the shear stress has also two peaks.

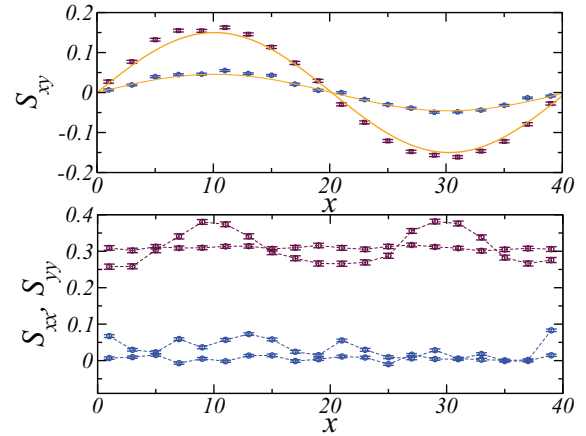


FIG. 7. (Color online) Profiles of components of the stress tensor for solidified and fluidized states with blue and maroon colors where amplitude of the external force has values $F_e = 7.6 \times 10^{-3}$ and 2.2×10^{-2} , respectively. Top: Profiles of the shear stress S_{xy} . The dashed lines show the predicted value by the theory. Bottom: Profiles of the diagonal components of the stress tensor S_{xx} and S_{yy} . In the fluidized state, the diagonal element of the stress tensor along the x direction S_{xx} is constant for both cases, but S_{yy} has two maxima at $x = 10$ and 30 where the shear stress has its maximal values. The packing fraction is $\phi = 0.7$, the aspect ratio of dimers is $\alpha = 1.8$, the number of dimers is $N = 819$, the capillary energy is $\varepsilon = 0.05$, and the system size is $L = 40$.

G. Density dependence of the solidification force

In Ref. [12], we have shown that, as a result of counterbalance of flux of the injected-dissipated power rates, the quantity $F_s L/8\varepsilon$ is independent of the system size (this is checked also for wet dimers in Sec. IV). Therefore, in the rest of this paper, we study the dependence of $F_s L/8\varepsilon$ on the packing fraction ϕ , the aspect ratio of dimers α , and the capillary energy ε . We again observe that for $\phi < 0.52$, the particles condense into two persistent shear bands, moving opposite to each other. These shear bands move with a constant velocity and sometimes collide and heat up the system. Furthermore, for $\phi > 0.52$, the system responds to the external force by developing an effective internal shear strength, while for $\phi < 0.52$ the yield stress cannot be attained. This crossover from a fluidized state into the persistent shear bands can be considered as a characteristic point in the phase diagram of wet granular matter, similar to the J point for frictionless disks (investigation of characteristics of such point, as a threshold for emergence of yield stress, is beyond the scope of this paper). On the other hand, for $\phi > \phi_{\text{rcp}}(\alpha)$, the confining pressure diverges and fluctuations of the order parameter Δv_y exceeds any reasonable limit. Therefore, we restrict our measurement to the range $0.52 < \phi < \phi_{\text{rcp}}(\alpha)$ (the value of $\phi_{\text{rcp}}(\alpha)$ depends on the aspect ratio of dimers α and is given at Ref. [9]).

Figure 8 shows dependence of the normalized solidification force $F_s L/8\varepsilon$ as function of the packing fraction ϕ . The black, red, and blue symbols correspond to the capillary energy $\varepsilon = 0.01, 0.05$, and 0.1 , and the aspect ratio $\alpha = 1.5, 1.2$, and 1.5 , respectively, where $\phi_{\text{rcp}}(1.2) = 0.877$ and $\phi_{\text{rcp}}(1.5) = 0.844$. The solidification force changes slightly at small ϕ and shows stronger dependence on the packing fraction ϕ in the dense region and diverges at the RCP. Based on our findings for wet

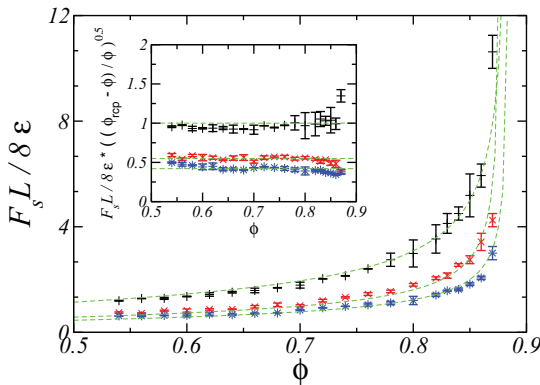


FIG. 8. (Color online) Dependence of $F_s L/8\varepsilon$ on the packing fraction ϕ . The black, red, and blue symbols correspond to values $\varepsilon = 0.01, 0.05$, and 0.1 , and $\alpha = 1.5, 1.2$, and 1.5 , respectively, where $\phi_{\text{rcp}}(\alpha = 1.2) = 0.877$ and $\phi_{\text{rcp}}(\alpha = 1.5) = 0.844$. The dashed lines show that the forces diverge as square root of $(\phi_{\text{rcp}} - \phi)/\phi$. Amplitude of the external force at solidification shows strong dependence on the packing fraction ϕ close to the RCP. Although the capillary force does not depend on the capillary energy, F_s weakly depends on the capillary energy ε . The reason is that before the transition, particles possess thermal-like motions. Inset shows that $F_s L/8\varepsilon((\phi_{\text{rcp}} - \phi)/\phi)^{1/2}$ takes roughly constant values. The chi-squared per degrees of freedom is $\chi^2 = 9.19745, 3.2096$, and 2.33998 for the top, middle, and bottom curves, respectively. The system size is $L = 20$.

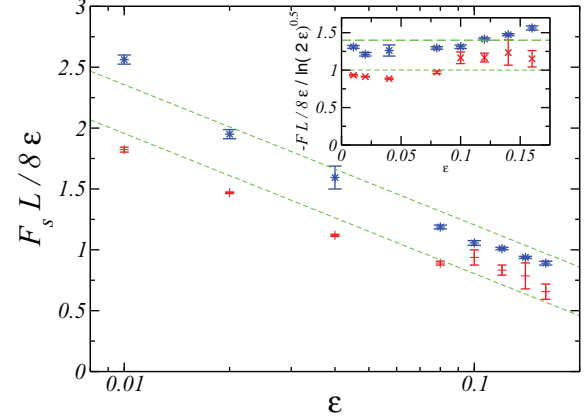


FIG. 9. (Color online) Amplitude of the external force at solidification $F_s L/8\varepsilon$ vs the capillary energy ε . The red and blue symbols correspond to $\phi = 0.7$, and 0.76 , respectively. The aspect ratio is $\alpha = 1.2$. The green dashed lines show the best logarithmic fits (the same dependence was found for wet disks). For both packing fractions, amplitude of the external force at solidification F_s increases on increasing the capillary energy ε . Inset shows that $F_s L/8\varepsilon / \ln \sqrt{2\varepsilon}$ takes roughly constant values for different ε . The reduced chi-squared per degrees of freedom is $\chi^2 = 14.3528$, and 13.3783 for the top and bottom curves, respectively. The system size is $L = 20$.

disks, we also expect to see the following dependence for wet dimers:

$$F_s L/8\varepsilon \sim \left(\frac{\phi_{\text{rcp}} - \phi}{\phi} \right)^{-\gamma}, \quad (10)$$

where γ is a positive exponent. As shown in the inset, the exponent is found to be $\gamma \simeq 1/2$. The quantity $1/(\phi_{\text{rcp}} - \phi)$ equals the free volume available in the system for two particles to pass. Since $\phi/(\phi_{\text{rcp}} - \phi)$ refers to the minimum number of particles that should be displaced in order to make a free volume for two particles to pass, the square-root scaling can be interpreted as the statement that passing of two particles triggers a small *microcrack* in the region which displaces $N_\phi^2 = \phi/(\phi_{\text{rcp}} - \phi)$ particles and ruptures N_ϕ capillary bridges.

Equation (10) has a prefactor that should depend on the capillary energy ε as well as the aspect ratio α . Figure 9 shows $F_s L/8\varepsilon$ as a function of the capillary energy. The red and blue symbols correspond to $\phi = 0.7$ and 0.76 , respectively, with the aspect ratio $\alpha = 1.2$. The system size is $L = 20$. The green dashed lines show the best logarithmic fit to the data and the inset demonstrates that $F_s L/8\varepsilon / \ln \sqrt{2\varepsilon}$ takes almost constant values.

H. Aspect ratio dependence of the solidification force and the master plot

Dependence of the prefactor of Eq. (10) on the aspect ratio is the last quantity to be examined. Figure 10 compiles our data for the amplitude of the external force at solidification $F_s L/8\varepsilon$, as a function of the aspect ratio. The red and blue symbols in Fig. 10 correspond to the packing fraction $\phi = 0.7$ and 0.76 , and the capillary energy $\varepsilon = 0.05$ and 0.01 , respectively. We see no systematic dependence of $F_s L/8\varepsilon$ on the aspect ratio for both data sets. Therefore, we conclude that the prefactor in Eq. (10) is dominated by the influence of the capillary bridges.

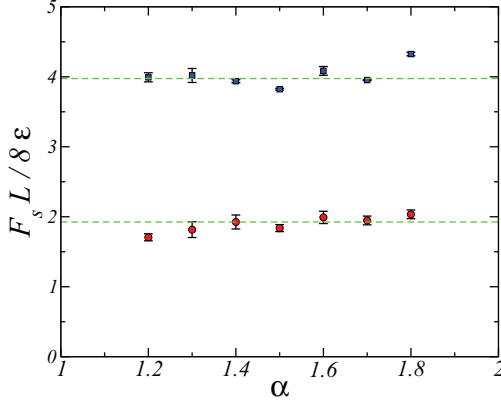


FIG. 10. (Color online) Amplitude of the external force at solidification $F_s L / \varepsilon$ vs the aspect ratio of dimers α . The red and blue symbols correspond to the packing fraction $\phi = 0.7$ and 0.76 , with the capillary energy $\varepsilon = 0.05$ and 0.01 , respectively. No systematic dependence of amplitude of the external force at solidification $F_s L / \varepsilon$ on the aspect ratio α is found. The mean value of the top curve is approximately 2.5 times larger than that of the bottom curve. The reason is that the top curve corresponds to a higher packing fraction. The reduced chi-squared per degrees of freedom is $\chi^2 = 1.19807$ and 18.19807 for the top and bottom curves, respectively. The system size is $L = 20$.

It is therefore relevant to express F_s as function of ϕ and ε in

$$F_s \simeq -C \frac{8\varepsilon}{L} \ln \sqrt{2\varepsilon} \left(\frac{\phi}{\phi_{\text{rcp}} - \phi} \right)^{1/2}, \quad (11)$$

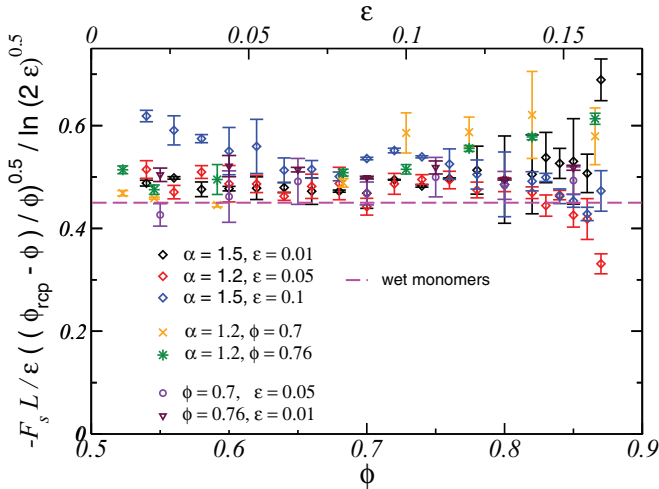


FIG. 11. (Color online) Ensemble of all data shown in Figs. 3, 4, and 5. The data collapse shows that amplitude of the external force at solidification F_s for wet dimers can well be described by Eq. (11) with prefactor of value $C = 0.55 \pm 0.05$. The light dashed line shows the previous data collapse for wet disks. This prefactor is larger than the one we previously reported for wet disks $B = 0.45 \pm 0.05$ (the dashed line), which demonstrates that wet dimers are stiffer than the wet disks. On the other hand, the dependence is exactly the same as the one we have found for wet disks. This implies that there is a possibility to find universalities on the mechanical response of wet granular material to the external forces.

where $C = 0.55 \pm 0.05$. The prefactor C is obtained from data collapse in Fig. 11. For the wet disks, we have found the prefactor $B = 0.45 \pm 0.05$, from a similar data collapse. This increase in the prefactor shows that wet dimers have a larger shear strength than wet disks.

IV. CONCLUSION AND OUTLOOK

The so-called jamming transition refers to development of yield stress in a granular system. Lemaître and Caroli studied dependence of the strain rate to the strain for frictionless bidisperse disks in a simple shear flow, and they found a continuous transition from the flowing regime to the arrested state [22]. Following that, we demonstrate here that existence of a network of capillary bridges makes such transitions discontinuous for both wet disks and wet rigid dimers. The reason for such a distinct behavior may be better understood if the reverse process, i.e., the solid-to-fluid transition, is considered. Let us consider a pile of granular materials on an inclined plane. It is well known that when the pile is dry, for inclination angles larger than the angle of repose, the pile fluidizes for any arbitrary small nonzero gravitational acceleration [23]. However, when the pile is wet, above the angle of repose, there exists a finite gravitational acceleration below which the system is enabled to bear the external force and stay in an arrested regime. The reason for such effect is originated from the existence of elementary networks of stretched capillary bridges [23]. The refluidization point F_f in Fig. 4 is analogous to the solid-to-fluid transition of a granular pile on an inclined plane. We see the same difference for the jamming transition, i.e., fluid-to-solid transition, of dry and wet particles where, in contrast to dry granulates, wet disks and dimers have a discontinuous solid-to-fluid transition of the strain rate (F_s in Fig. 4). These qualitative and quantitative differences in the solid-to-fluid and fluid-to-solid transitions in sheared wet granular material make them drastically distinct from that of sheared dry frictionless granular materials. In fact, our study shows that the discontinuity nature of such transitions in wet granular materials does not depend on the shape of particles and both disks and dimers share that common feature.

We have also investigated the jamming phase diagram of wet dimers and have compared it with the one reported previously for wet disks [12]. Although wet dimers are found to be more stiffer than the wet disks, we have found that the structure of the jamming phase diagram does not change as we consider wet dimers. This implies that the scaling relation among the amplitude of the external force at solidification F_s , the packing fraction ϕ , and its logarithmic dependence on the capillary energy ε are universal features of mechanical response of wet granular material to the external forces, independent of the granular shape. Interestingly, we have found that the arrest stress of wet dimers is independent from the aspect ratio α .

Analogously with the J point in the jamming phase diagram of dry spheres, we have discovered that there exists a characteristic point at around $\phi \simeq 0.52$, where the system crosses over from a nonergodic shear banding regime into an ergodic yield stress state. This point is also independent from the particle shape, and we have observed it for both wet disks

and dimers. More study needs to be done to reveal if this point is universal and it is independent from the driving mechanism. In dry frictionless disks, there exists a characteristic point at the packing fraction equal to $\phi_p \simeq 0.55$, where the probability to obtain a systemwide spanning cluster maximizes [24]. The difference between our observation and the one reported in the aforementioned reference is that in the former for $\phi > 0.52$ the system has a finite arrest and yield shear stress; in contrast, in the latter the system is enabled to develop yield stress only at the J point, $\phi_{\text{rep}} = 0.84$, which is well above the percolation point $\phi_p \simeq 0.55$.

The next serious question is to inquire if the mechanical properties of wet convex particles, such as wet ellipsoids, can be grouped within the same universality class of wet concave particles (e.g., wet dimers). Further investigation of this hypothesis is of great importance as we deal in reality with particles that have nonspherical shapes. Our naive expectation for this question is that the yield stress of wet granular materials should be independent of the concavity or convexity of the particles. The reason is that we have demonstrated that the structure of the jamming phase diagram for both wet disks (convex) and wet dimers (concave) bear the common features. As a result, there the hope to find a universality in this respect.

Results of this line of research can have broad consequences for many disciplines, e.g., petroleum engineering. Despite advances in oil recovery technology, no more than two-thirds of an oil field can be extracted. An international group of scientists contributed to an enhanced oil recovery research program (EOR-ExploRe) for the British Petroleum energy company. The aim was to increase the recovery of oil by 10%. In an oil field, the oil is distributed within a porous medium, and our current understating about such a system is limited to physics of a mixture of two simple fluids distributed within spherical beads. But in the oil fields, rocks and beads with complicated shapes are suspended in a complex fluid [25]. These two research subjects will be the active avenues for state-of-the-art research over the next few decades. Despite the excessive complications of studying oil fields, the universal properties emerging from the study of complex systems are the only hope to set up a satisfactory physical model for such a system. In this respect, understanding the mechanical properties of external forces on wet irregular beads is an urgent task.

ACKNOWLEDGMENTS

We express our gratitude to S. Herminghaus, J. Vollmer, and M. Brinkmann for the inspiring discussions that led us to work on this project. We are thankful for the comments from anonymous referees which increased the quality of the paper and the presentation of the results. We are also grateful to M. Akbari-Moghanjoughi, A. Abbasi, and M. Habibi for enlightening discussions. This project was financially supported by INSF Project No. 90004064.

APPENDIX

1. System-size dependence of the critical force

In order to get more insight into the solidification transition and its dependence on the system size L , we assume a creeping flow $v_y(x)$ at the onset of solidification. The power injected by

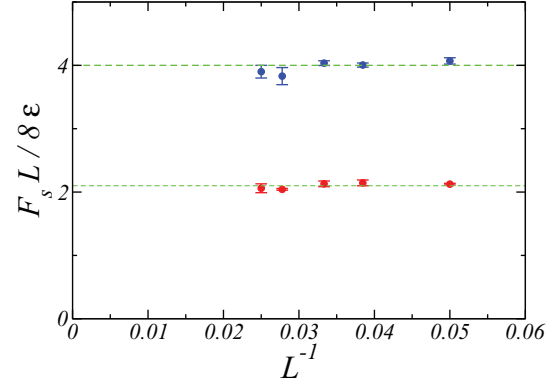


FIG. 12. (Color online) Amplitude of the external force at solidification, $F_s L / 8 \epsilon$, as function of the inverse of the system size for packing fraction $\phi = 0.7$ (lower line) and $\phi = 0.8$ (upper line). For both curves, the aspect ratio of dimers is $\alpha = 1.8$ and the capillary energy is $\epsilon = 0.05$. The mean value of the green line for both cases can be interpreted as the number of capillary bridges that should be ruptured in order to let one particle displace one unit of length.

the external force is given by

$$\langle P_{\text{inj}} \rangle = \int_0^L v_y(x) F_e(x) n(x) dx, \quad (\text{A1})$$

where $n(x)$ is the number of particles in a rectangle of $L \times dx$ along the flow direction. We approximate the velocity profile by its first even harmonic,

$$v_y(x) = \Delta v_y \cos\left(\frac{2\pi x}{L}\right). \quad (\text{A2})$$

Accordingly, the estimated injection rate can be written as

$$\langle P_{\text{inj}} \rangle = N \frac{\Delta v_y F_e}{2}. \quad (\text{A3})$$

The dissipation rate due to rupture of the capillary bridges can be given by

$$\langle P_{\text{diss}} \rangle = \int_0^L n(x) \dot{\gamma}(x) \nu \epsilon dx = N \frac{4\nu \epsilon \Delta v_y}{L}, \quad (\text{A4})$$

where $\dot{\gamma}(x)$ is the local shear rate at position x and ν is the average number of capillary bridges per particle.

In the stationary state and very close to the solidification point, and as a consequence of the balance of injection and dissipation rates, we obtain

$$F_s = \frac{8\nu \epsilon}{L}. \quad (\text{A5})$$

F_s can be interpreted as the minimum force that keeps the system in a flowing regime. One may conclude from Eq. (A5) that (i) $F_s L / 8 \epsilon$ is a dimensionless quantity that is independent of the system size and (ii) the amplitude of the external force at the solidification F_s scales with the inverse of the system size. This theoretical prediction has been checked for different system sizes $L = 20, 26, 30, 36$, and 40 for two packing fractions $\phi = 0.7$ and 0.8 by the red and blue symbols, respectively (Fig. 12). In these simulations, the aspect ratio of dimers is 1.8 , and the capillary energy is $\epsilon = 0.05$. In the figure $F_s L / 8 \epsilon$ is plotted versus the inverse of the system size L . Both predictions by Eq. (A5) have been verified by the simulations.

- [1] A. J. Liu and S. R. Nagel, *Nature* **396**, 21 (1998).
- [2] C. S. O'Hern, L. E. Silbert, A. J. Liu, and S. R. Nagel, *Phys. Rev. E* **68**, 011306 (2003).
- [3] P. Olsson and S. Teitel, *Phys. Rev. Lett.* **99**, 178001 (2007).
- [4] M. P. Ciamarra, R. Pastore, M. Nicodemi, and A. Coniglio, *Phys. Rev. E* **84**, 041308 (2011).
- [5] C. S. O'Hern, S. A. Langer, A. J. Liu, and S. R. Nagel, *Phys. Rev. Lett.* **86**, 111 (2001).
- [6] I. Zuriguel and T. Mullin, *Proc. R. Soc. Lond. A* **464**, 99 (2008).
- [7] M. Z. Miskin and H. M. Jaeger, *Nature Materials* **12**, 326 (2013).
- [8] M. Mailman, C. F. Schreck, C. S. O'Hern, and B. Chakraborty, *Phys. Rev. Lett.* **102**, 255501 (2009).
- [9] C. F. Schreck, N. Xub, and C. S. O'Hern, *Soft Matter* **6**, 2960 (2010).
- [10] S. Herminghaus, *Adv. Phys.* **54**, 221 (2005).
- [11] S. Strauch and S. Herminghaus, *Soft Matter* **8**, 8271 (2012).
- [12] S. H. Ebrahimpazhad Rahbari, J. Vollmer, S. Herminghaus, and M. Brinkmann, *Phys. Rev. E* **82**, 061305 (2010).
- [13] D. J. Hornbaker, R. Albert, I. Albert, A. L. Barabási, and P. Schiffer, *Nature* **387**, 765 (1997).
- [14] Ch.D. Willet, M. J. Adams, S. A. Johnson, and J. P. K. Seville, *Langmuir* **16**, 9396 (2000).
- [15] S. Nowak, A. Samadani, and A. Kudrolli, *Nat. Phys.* **1**, 50 (2005).
- [16] N. Mitarai and F. Nori, *Adv. Phys.* **55**, 1 (2006).
- [17] M. Scheel *et al.*, *Nat. Mat.* **7**, 189 (2008).
- [18] T. Pöschel and T. Schwager, *Computational Granular Dynamics* (Springer, New York, 2005).
- [19] A. Donev, *Science* **303**, 990 (2004).
- [20] F. H. Stillinger and B. D. Lubachevsky, *J. Stat. Phys.* **73**, 497 (1993).
- [21] See Supplemental Material at <http://link.aps.org/supplemental/10.1103/PhysRevE.88.042203> for two movies of our simulations for the solidified and fluidized states.
- [22] A. Lemaître, and C. Caroli, *Phys. Rev. Lett.* **103**, 065501 (2009).
- [23] S. H. Ebrahimpazhad Rahbari, J. Vollmer, S. Herminghaus, and M. Brinkmann, *Europhys. Lett.* **87**, 14002 (2009).
- [24] T. Shen, C. S. O'Hern, and M. D. Shattuck, *Phys. Rev. E* **85**, 011308 (2012).
- [25] GeoMorph - Göttingen exploration of Microscale oil reservoir physics, <http://www.dcf.ds.mpg.de/index.php?id=863>.